



<b>Publication Year</b>	2016
<b>Acceptance in OA</b>	2020-05-14T16:04:14Z
<b>Title</b>	PSF modeling by spikes simulations and wings measurements for the MOONS multi fiber spectrograph
<b>Authors</b>	LI CAUSI, Gianluca, Lee, D., VITALI, Fabrizio, Royer, F., OLIVA, Ernesto
<b>Publisher's version (DOI)</b>	10.1117/12.2232964
<b>Handle</b>	<a href="http://hdl.handle.net/20.500.12386/24838">http://hdl.handle.net/20.500.12386/24838</a>
<b>Serie</b>	PROCEEDINGS OF SPIE
<b>Volume</b>	9908

# PROCEEDINGS OF SPIE

[SPIDigitalLibrary.org/conference-proceedings-of-spie](https://spiedigitallibrary.org/conference-proceedings-of-spie)

## PSF modeling by spikes simulations and wings measurements for the MOONS multi fiber spectrograph

Li Causi, G., Lee, D., Vitali, F., Royer, F., Oliva, E.

G. Li Causi, D. Lee, F. Vitali, F. Royer, E. Oliva, "PSF modeling by spikes simulations and wings measurements for the MOONS multi fiber spectrograph," Proc. SPIE 9908, Ground-based and Airborne Instrumentation for Astronomy VI, 99088P (9 August 2016); doi: 10.1117/12.2232964

**SPIE.**

Event: SPIE Astronomical Telescopes + Instrumentation, 2016, Edinburgh, United Kingdom

# PSF modeling by spikes simulations and wings measurements for the MOONS multi fiber spectrograph

Li Causi G.\*<sup>a</sup>, Lee D.<sup>b</sup>, Vitali F.<sup>a</sup>, Royer F.<sup>c</sup>, Oliva E.<sup>d</sup>

<sup>a</sup>INAF-Osservatorio Astronomico di Roma, Via Frascati 33, Monteporzio Catone, Roma, Italia;

<sup>b</sup>STFC UK Astronomy Technology Centre, Royal Observatory, Edinburgh, Blackford Hill, Edinburgh, EH9 3HJ; <sup>c</sup>GEPI, Observatoire de Paris-CNRS-Université Paris Diderot, 5 Place Jules Janssen, F-92195 Meudon Cedex, France; <sup>d</sup>Osservatorio Astrofisico di Arcetri, Largo Enrico Fermi 5, I-50125, Firenze, Italia

## ABSTRACT

The optical design of MOONS, the next generation thousand-fiber NIR spectrograph for the VLT, involves both on-axis reflective collimators and on-axis very fast reflective cameras, which yields both beam obstruction, due to fiber slit and detector support, and image spread, due to propagation within detector substrate. The need to model and control i) the effect of the diffraction spikes produced by these obstructions, ii) the detector-induced shape variation of the Point Spread Function (PSF), and iii) the intensity profile of the PSF wings, leads us to perform both simulations and lab measurements, in order to optimize the spider design and built a reliable PSF model, useful for simulate realistic raw images for testing the data reduction. Starting from the unobstructed PSF variation, as computed with the ZEMAX software, we numerically computed the diffraction spikes for different spider shapes, to which we added the PSF wing profile, as measured on a sample of the MOONS VPH diffraction grating. Finally, we implemented the PSF defocusing due to the thick detector (for the visible channel), we convolved the PSF with the fiber core image, and we added the optical ghosts, so finally obtaining a detailed and realistic PSF model, that we use for spectral extraction testing, cross talk estimation, and sensitivity predictions.

**Keywords:** MOONS, diffraction spikes, PSF wings profile, VPHG, detector defocus

## 1. INTRODUCTION

The next generation high performance spectrographs under design for current and future large telescopes are complex instruments which promise to win several technical challenges, like imaging thousands of simultaneous spectra, reaching a photon limited sky subtraction, and gaining excellent instrument calibration for grasping very faint sources.

In order to test the fulfillment of such strict requirements, realistic end-to-end data simulator codes are needed, based on accurate Point Spread Function (PSF) models, which includes all the relevant effects along the full information path from the astronomical source to the detector readout.

This work describes the way we perform such PSF computation in the “Virtual MOONS”<sup>[1]</sup> end-to-end simulator for the MOONS spectrograph, and the design optimizations that we derived.

### 1.1 The instrument

MOONS, which stands for “Multi Object Optical and Near-infrared Spectrograph for the VLT”<sup>[2]</sup>, is the next generation fibre-fed, optical to near-IR, multi-object spectrograph designed to use the full 25 arcmin diameter field of view (FoV) of one of the Unit Telescopes (UT) of the VLT at the European Southern Observatory (ESO) in Paranal Chile. The operating wavelength for MOONS is 0.645 $\mu$ m to 1.8 $\mu$ m, and both medium and high-resolution spectroscopy is offered. In the medium-resolution mode (R~4,000-6,000), the entire 0.645-1.8 $\mu$ m range is observed simultaneously, for extragalactic redshift survey, while the high-resolution mode covers three selected regions in visible band, with R>9,000 around the CaT region to measure stellar radial velocities, and R~19,000 in the H-band, for detailed measurements of

---

\*gianluca.licausi@inaf.it

chemical abundances. The front end of the instrument will sample the telescope FoV with 1024 finely movable fibers, whose light is fed into a couple of identical, cryogenic, triple arm spectrographs mounted on the instrument Nasmyth platform. The two spectrographs are mounted on the opposite sides of a vertical optical bench, housed in a single cryostat. In each spectrograph the light from 512 fibers, arranged in a pseudo-slit, is collimated by an on-axis parabola and then split into three channels (RI, YJ and H spectral bands), using two dichroic mirrors. The beam is then dispersed, and finally focused by a fast  $f/0.95$  reflective camera<sup>[3]</sup> onto a  $4k \times 4k$  detectors in each channel, an LBNL  $250\mu\text{m}$  thick full depletion CCD<sup>[7]</sup> for the visible beam, and two Teledyne H4RG HgCdTe<sup>[8]</sup> arrays for the infrared channels (Figure 1).

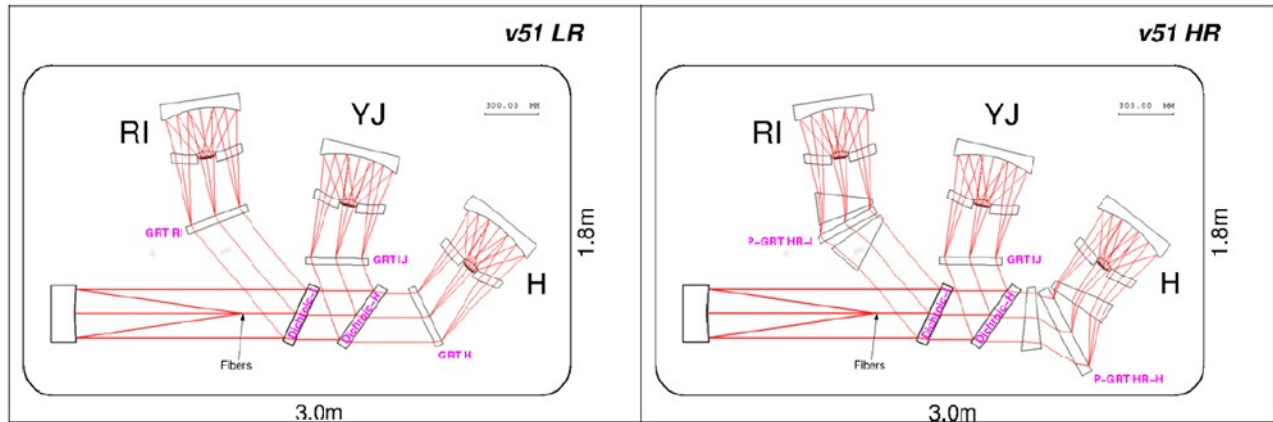


Figure 1: layout of one of the two MOONS spectrographs. Left panel: set-up for the medium-resolution configuration; Right panel: high-resolution configuration.

## 1.2 The end-to-end simulator

To establish the expected performance of MOONS, we have developed the “Virtual MOONS”<sup>[1]</sup> code in IDL language<sup>[5]</sup> in order to produce end-to-end quantitative simulations which, starting from the intrinsic source spectra, produce fully realistic raw detector images (Figure 2).

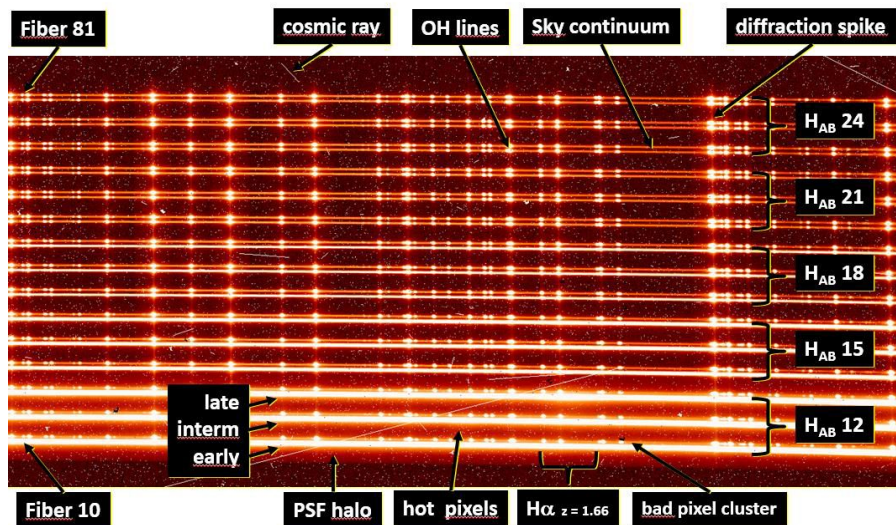


Figure 2: End-to-end simulation of a raw H-band MOONS frame. The slit is aligned vertically and the spectra are dispersed in the horizontal direction. Only the 2D spectra for a sub-set of fibres are shown, for galaxies of different spectral types (early, intermediate and late) and a range of  $H_{AB}$  magnitudes.

The simulations include all geometric and diffraction variations in the PSF, as well as optical distortions, spectrograph efficiencies, fiber transmissions, grating efficiencies, and descriptions of the detector illumination, stray light, and thermal background, to calculate the expected photon counts per pixel on the array. Typical cosmetics and localized defects of the detectors, like bad pixels, dust, cosmic rays, and other effects are also included.

## 2. OPTICAL ABERRATIONS

The first step of our PSF computation is the generation of a 4D data cube, for each spectral mode, containing the optical aberration shapes, as produced by the optics for a grid of fiber positions along the pseudo-slit, and wavelengths along the spectral range. We accomplish this task by directly querying the “Huygens PSF” aberration figure to the ZEMAX<sup>[6]</sup> optical design from inside IDL, thanks to the zmxIDL code from L. Busoni<sup>[4]</sup>, which adopt the DDE protocol of the Windows™ operating system. The basic mechanism of this communication consists in sending string commands to ZEMAX and receiving a string answer containing numeric values, or a confirmation that a data file has been written.

As shown in Figure 3, the aberration spot shape is highly variable across the focal plane, so that a fine grid is necessary for a subsequent good interpolation to any pixel position and hence 9 field and 9 wavelengths are used .

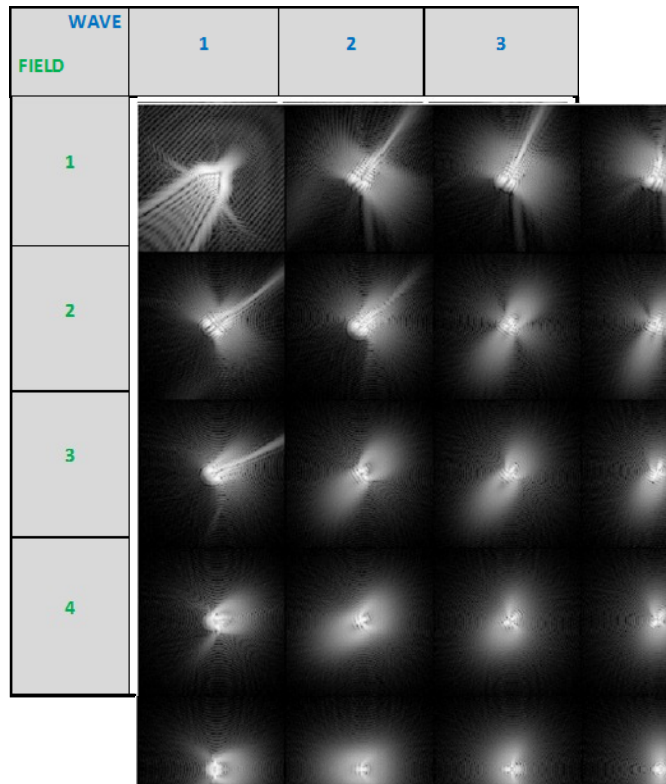


Figure 3: Part of the Huygens PSF grid for the H spectral mode (logarithmic grayscale, 128 $\mu$ m size).

### 3. PSF HALO

#### 3.1 Expected wing profile

The Huygens PSF images shown in Figure 3 only accounts for the part of the PSF very close to its central peak, but do not describe the PSF profile at large distance, whose flux causes the well-known wings aside the bright OH sky lines in the near-infrared (NIR) spectra, partially responsible for the false continuum emission detected among these.

OH lines are numerous and bright emission lines<sup>[9]</sup>, caused by the airglow emission of the high atmosphere, which accounts for the largest part of the night sky brightness between I and K spectral bands. Due to the high intensity, the tiny fraction of their flux falling into the PSF wings can severely increase the true sky continuum, so it is important to model this profile for simulating how it affects the instrument performances.

The PSF halo profiles, shown in the literature for some working spectrographs, often exhibits a wide behaviour, which can be fit by a two-component Lorentzian function, like e.g. in the FIRE/Magellan<sup>[10]</sup> and APOGEE<sup>[11]</sup> spectrographs (see Figure 4). This may depend on many factors, like imperfections on the grating ruling, diffuse scattering on the surfaces of optical elements or within the optical materials, diffraction spikes overlapping the dispersion direction, or optical ghosts, and in our computation we need to consider these effects separately.

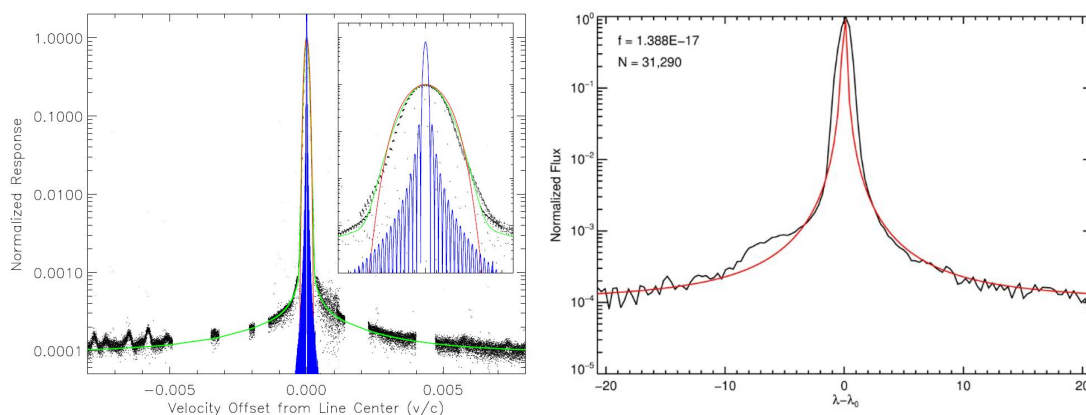


Figure 4: Wide PSF profiles, along the spectral direction, for the FIRE/Magellan spectrograph (left) and the APOGEE spectrograph (right), from Sullivan et al. 2012<sup>[10]</sup> and Wilson J.C., et al.<sup>[11]</sup>, respectively.

If we had pure diffraction, we expect to have a circular Airy (i.e. Bessel  $J_1$ ) profile for the wings, asymptotically decreasing as  $r^{-3}$  in both spatial and spectral directions, as also results from our analytical computation of the Fraunhofer diffraction from a linear grating hit by a circular beam<sup>[12]</sup>. We assumed for this calculation a circular pupil and a flat-top profile for the illumination of the spectrograph pupil, i.e. a uniform angular profile for the intensity exiting from the 150 $\mu$ m fiber output. Such expectation should reveals true if the internal diffusion of optical material is negligible, and if the grating does not produce stray light, that is what we measured in the lab as described in the following section.

#### 3.2 Lab measurements

The MOONS spectrograph will use either a volume phase holography (VPH) grating, or a lithographic one. In order to measure the possible contribution to the PSF profile of a VPH disperser, we built an optical bench with the aim to compare the spot produced by a point source at the first diffraction order with the reference spot it produces without the grating.

In order to achieve a clean detection of the faint PSF wings, we prepared an optical bench whose optical train has only two plano-convex lens, to minimize the number of ghosting surfaces. Then we put one iris diaphragms on the rear side of each of them, and close all the optics into a light-tight box. The source is a He-Ne laser that we located outside, whose light is carried by a mono-modal optical fiber at the collimator focus. The detector, an ALTA U9000 CCD camera<sup>[12]</sup>, is

placed on a rotating base together with the camera lens, in order to be alternatively aligned to the direct beam, or to the first order diffraction beam. In the latter configuration a custom 750 lines/mm VPH grating<sup>[12]</sup> (courtesy by A. Bianco) is inserted in the optical path, centered on the pivot of this rotating base (Figure 5). For each of the two configurations, we acquire a large number of background images, and subtract them from the same number of point source images, exposed with the same integration time.

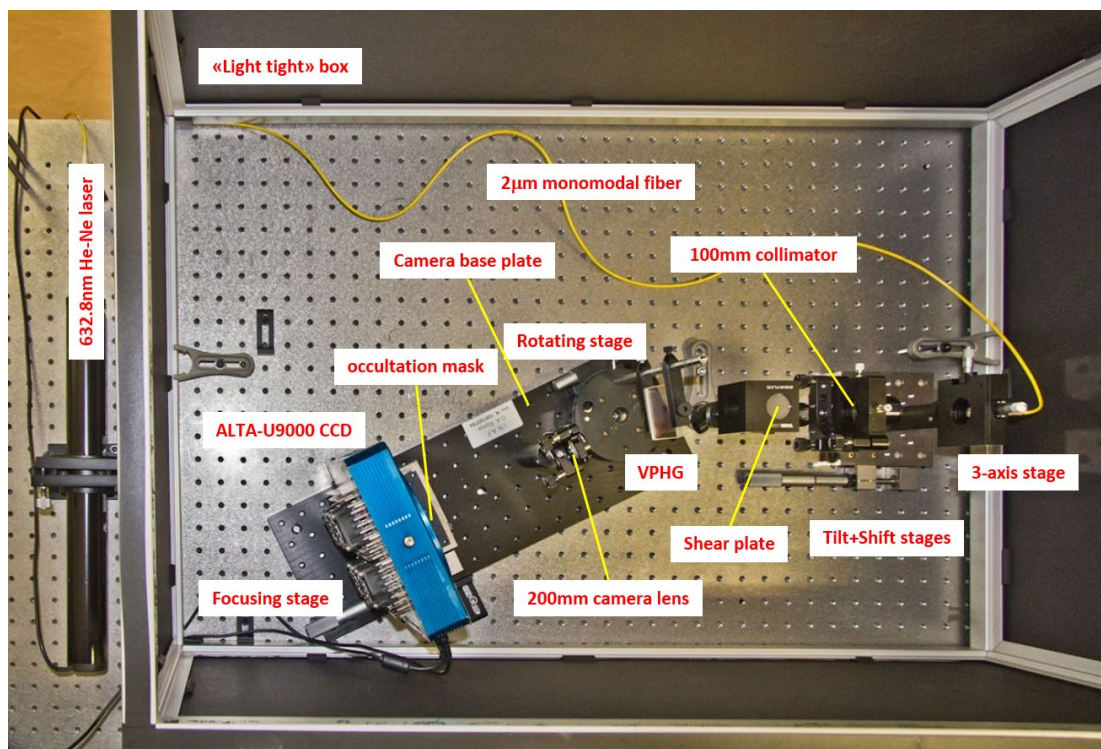


Figure 5: The optical bench for the measurements of the PSF wings profile, in the configuration of first diffraction order.

We soon recognized an intense multiple reflection ghost formed by the multiple reflections between the CCD pixels grid and the CCD optical window, which produces the intense regular pattern clearly seen in Figure 6 and clearly covers the true PSF halo profile. We thus decided to intercept the bright central peak with an occultation mask in order to avoid such ghost (Figure 6, right), and finally acquire the halo images with and without the VPH grating. Their radial profile are displayed in Figure 7.

In conclusion, our measurement shows that there is no evidence of light diffusion to the PSF wings due to the VPH disperser. The halo intensity decreases as  $r^{-3}$  in the closer part, just outside the occultation mask, and as  $r^{-2}$  in the outer region, and this profile is the same for both spatial and spectral direction, actually being circularly symmetric.

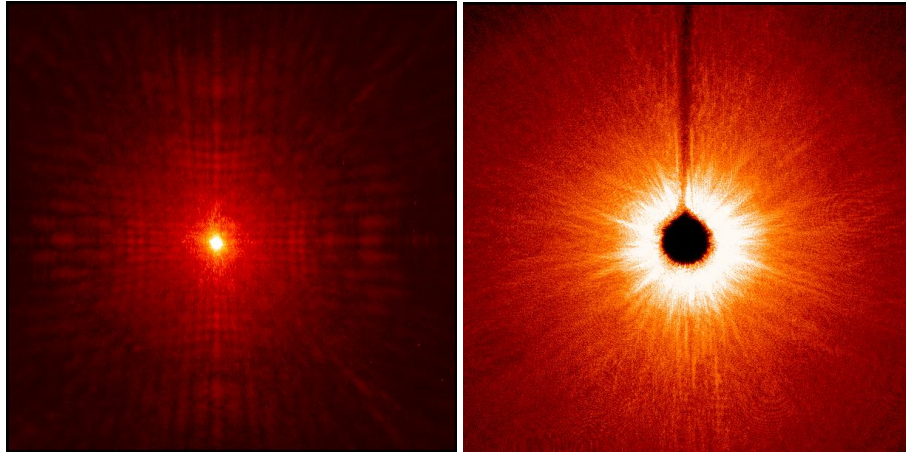


Figure 6: Left: pattern of the multiple reflections of the peak between detector surface and detector window. Right: PSF with central obscuration to avoid the multiple reflections of the central peak.

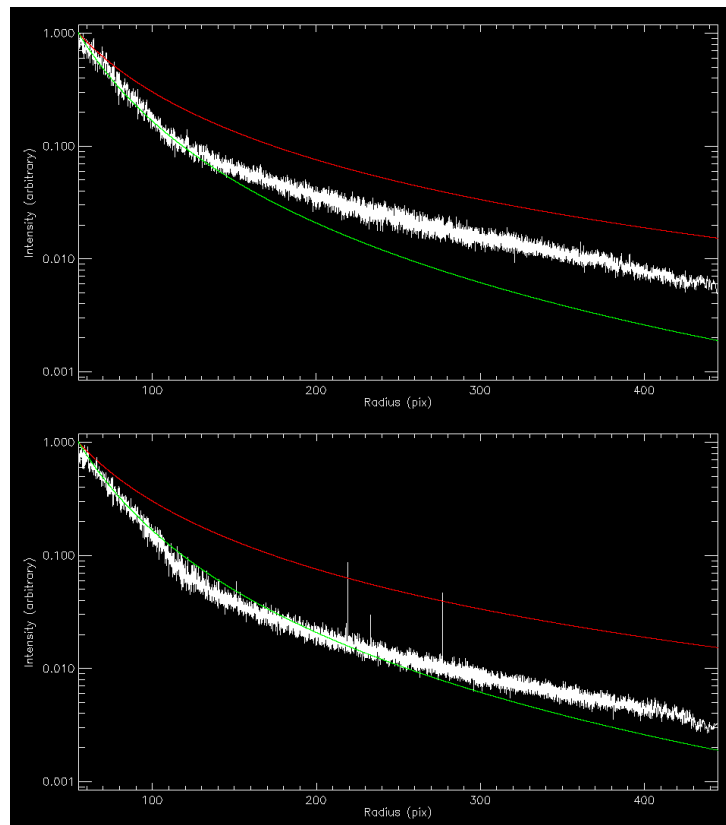


Figure 7: Radial profiles of the PSF wings outside the occultation mask without VPH (top) and with VPH at first order (bottom). The red and green lines are respectively the rescaled  $r^{-2}$  and  $r^{-3}$  behavior. The two profiles are very similar, confirming that there is no evidence of light diffusion to the PSF wings due to the VPH disperser.

## 4. DIFFRACTION

### 4.1 Diffraction spikes

So far, we have analyzed the PSF shape produced by a uniform circular pupil, but the real pupil in MOONS will be obstructed by several elements, due to the reflective on-axis collimator and camera, namely the fiber slit assembly, and the detector box with its spider arms, whose presence modifies the ideal Airy diffraction figure, and generates diffraction spikes.

Optics theory says that any flat edge in the pupil produces a diffraction spike, which extends along the orthogonal direction to the edge, with an intensity asymptotically decreasing as  $r^{-2}$ . This means that the presence of any vertical edge in the beam like the fiber slit, the lateral side of detector box, or a vertical arm in the spider, will produce a horizontal diffraction spike, which overlaps to the spectral direction producing the false continuum among the OH lines, as explained by Figure 8.

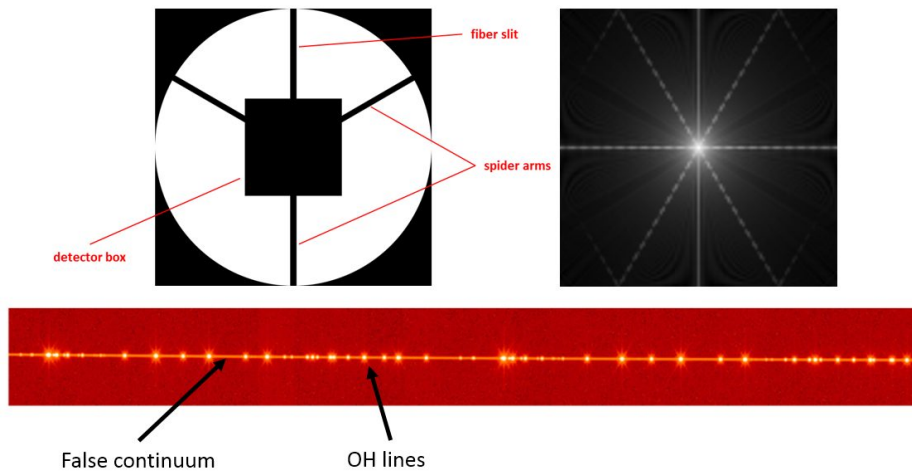


Figure 8: The sample pupil obstruction due to a vertical fiber slit, a square detector, box and a three-arm spider (top left) produces various diffraction spikes in the PSF at focal plane (top right). The horizontal spikes coming out from the bright OH lines are due to the vertical edges in the obstruction, and they overlap to the spectral direction producing a bright false continuum (bottom).

### 4.2 Obstruction re-shaping

In order to avoid this contamination along the spectra and also with the aim to reduce possible cross talk between adjacent fibers due to spread of light in the spatial direction, we optimally re-shaped the beam obstruction in order to only involve the three definite edge angles of  $0^\circ$  and  $\pm 80^\circ$ , as shown in Figure 9, left panel.

The diffraction spikes produced by this pupil, as computed by a fast Fourier transform (FFT), presents only two thick spikes inclined of  $\pm 10^\circ$ , and one narrow spike strictly aligned along spatial direction, thus avoiding both the overlapping with the spectral trace, and the fiber cross talk at different wavelengths. We also carried lab measurements with a very simple, hand-cut, pupil mask in order to prove that the proposed shape effectively splits the horizontal diffraction spikes in two parts, as illustrated in Figure 10.

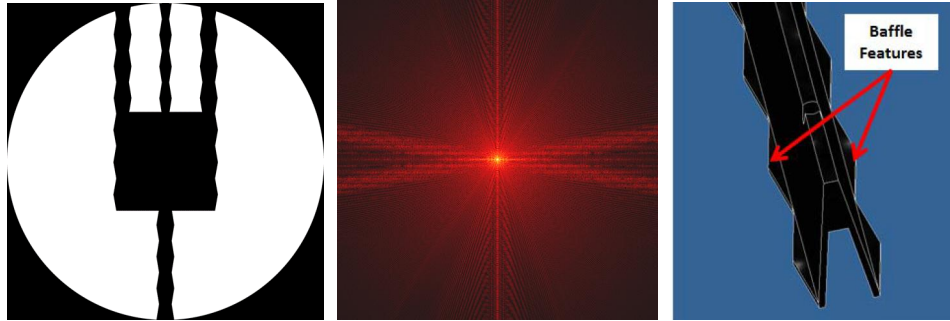


Figure 9: Optimized obstruction shape for MOONS: both the fiber slit, the two-rib fork spider which holds the square detector box, and the lateral side of detector box itself, are masked with a  $10^\circ$  triangular wave profile (left), in order to split the horizontal diffraction spikes so avoiding overlapping to the spectral trace (middle). Mechanical design of the spider mask is shown in right panel.

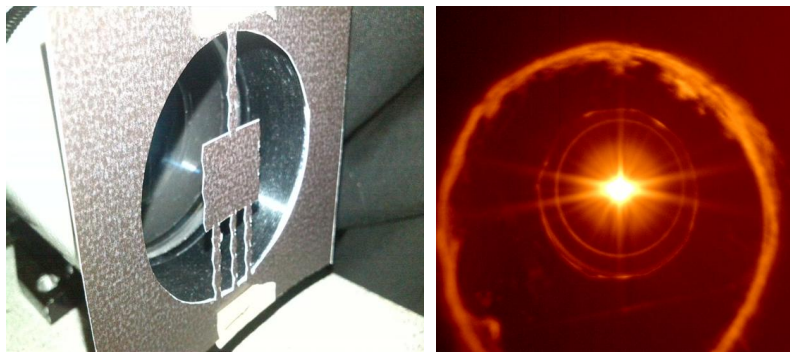


Figure 10: Lab test to confirm the diffraction shape shown in central panel of Figure 9. Left panel: hand cut obstruction mask at the entrance of the test camera; right panel: resulting diffraction spikes.

We thus introduced this new obstruction shape into the Virtual MOONS simulator, and computed its projection for a grid of off-axis positions, thus building the 4D pupils cube, corresponding to the fields and wavelengths already adopted. This projection also consider the varying elliptical shape of the beams for the different angles, and the matrix of beam vignetting (which spans e.g. from 20% to 26% for H channel). The corresponding diffraction images are computed with FFT, and are then resized to the same resolution of the Huygens PSFs to be merged with them into a comprehensive 4D aberration-plus-diffraction image cube (Figure 11).

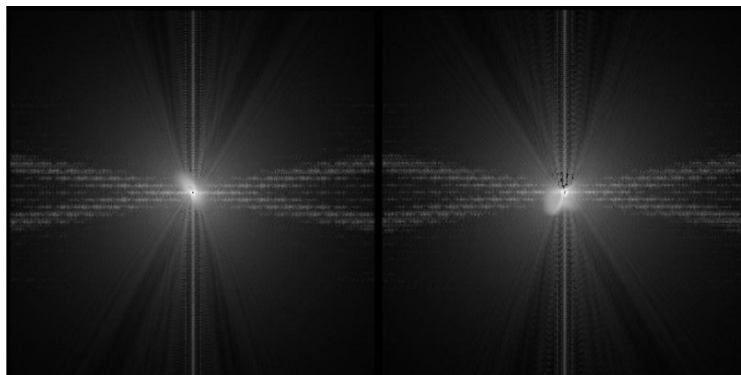


Figure 11: Diffraction-plus-aberration PSF for two fiber different positions and wavelength.

## 5. DETECTOR CONTRIBUTION

### 5.1 Optical effects

At wavelengths greater than approximately 900nm, the quantum efficiency of Silicon CCDs is known to rapidly fall, due to the increase in absorption depth of the silicon substrate. The use of a thick CCD, with substrate thickness greater than 100 $\mu\text{m}$ , is therefore required for the visible channel of MOONS in order to maintain high efficiency. However, as the optical beam passes through the thick CCD it gradually diverges, as shown in Figure 12, resulting in an extra blurring of the final PSF.

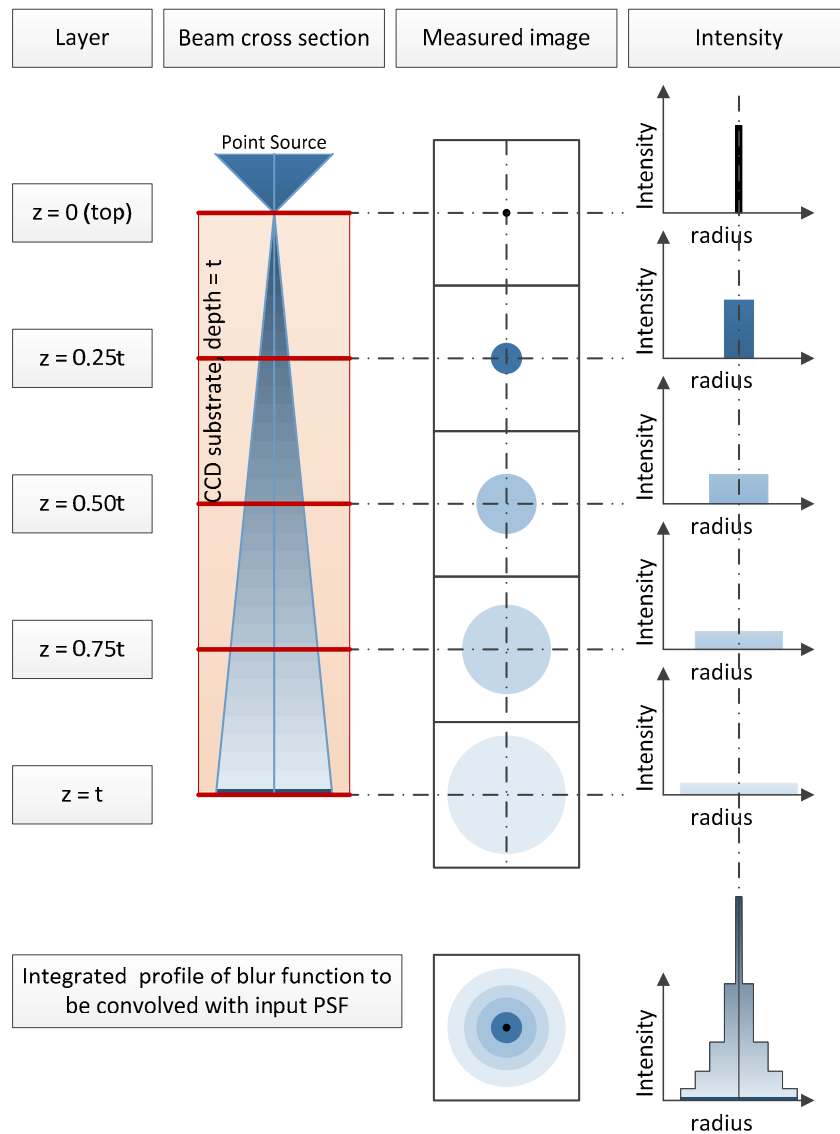


Figure 12 Schematic of the process of beam divergence in a thick CCD.

We model this effect of beam divergence by using both ZEMAX, to perform PSF simulations for a set of layers at various depths within the Silicon, and IDL to perform a weighted sum of the layers thus obtaining the final PSF, as measured by the CCD. This process is illustrated schematically in Figure 12, using 5 layers for simplicity.

An example of the PSF defocusing at three depth layers, generated using the geometric image analysis feature of ZEMAX for an on-axis 150 $\mu\text{m}$  fiber at 931nm, is shown in Figure 13. We see that, as the depth in the silicon increases, the image blurs, while the peak intensity decrease and the centroid moves to the left, due to the entering angle of the off-axis beam. For the example shown in Figure 13, the predicted radial blurring of the measured PSF is 7% resulting in a small reduction to the spectral resolving power.

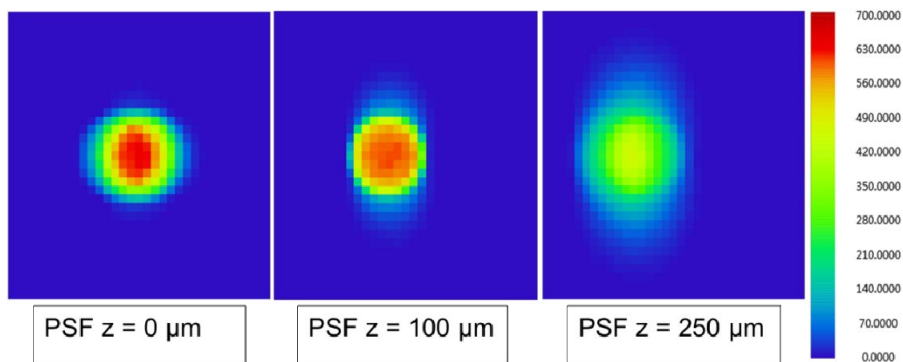


Figure 13 CCD induced defocusing simulation, for an on-axis spot at 931nm, at three depth layers within a thick CCD. The size of the blue box is 165 $\mu\text{m}$ , and the pixel size is 5 $\mu\text{m}$ .

## 5.2 Electronic effects

When a photon is absorbed within a CCD's silicon substrate it generates an electron which then moves towards the collection region of the CCD pixel under an applied voltage. As the electron moves through the silicon, it can drift into a neighboring pixel if the applied voltage is not sufficient to move it quickly to the collection region. This effect, known as lateral charge diffusion, causes the measured PSF to broaden and, for a fixed voltage, becomes worse with sensor thickness. A full description of the diffusion process, and how to calculate the corresponding PSF blurring, is given in O'Connor et al. 2006<sup>[15]</sup>. We use O'Connor procedure to compute this effect and we find a spread of 4 $\mu\text{m}$  RMS at 650nm for the 250 $\mu\text{m}$  thick MOONS CCD operated at 100V. In comparison, a 100 $\mu\text{m}$  thick CCD has a charge diffusion of 1.6 $\mu\text{m}$  RMS.

A similar effect, due to both charge diffusion and inter-pixel capacitance, is also present in the thin infrared CMOS, causing a cross talk to neighboring pixels, for which we adopt the H4RG-15 data sheet value of 2.42% diffusion into the nearest pixels<sup>[8]</sup>.

## 6. OPTICAL GHOSTS

At this point, we only miss to add the optical ghost, which are combinations of defocused replicas of the focal plane image, produced by multiple reflections within the optical surfaces.

Currently we compute the ghosts from outside the Virtual MOONS code. We performed an optical analysis of the scattered and stray light performance of the MOONS spectrograph using the non-sequential ray-tracing software TracePro<sup>®</sup>. A picture of the TracePro optical model, showing only the optical components, is shown in Figure 14, with the red rays indicating the path of the YJ-band light. The model also contains the spectrograph opto-mechanical hardware.

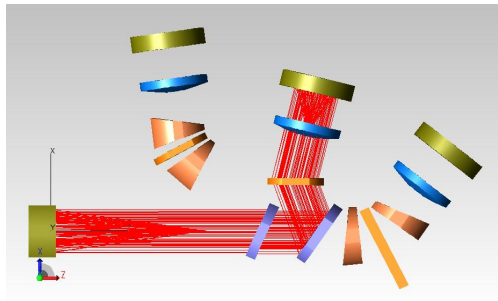


Figure 14 Optical ray-trace diagram for the YJ-band of the MOONS spectrograph.

We then analyzed the TracePro model to check for the presence of in focus ghost images, stray light paths, and to predict the overall level of background stray light reaching the detector. The relative intensity of stray light and location of ghost images is then included in the MOONS PSF performance model. The various optical and mechanical surfaces within the model were defined to have realistic surface treatments, such as anti-reflection coatings with a reflectivity of 1% and baffle structures with 90% absorption.

The optical design of the MOONS spectrograph camera<sup>[9]</sup>, with lens 2 embedded within the larger lens 1, can potentially result in a number of ghost images where light passes through the mounting interface between lenses 1 and 2. To test this we performed a non-sequential optical ray-trace with illumination from an on-axis fiber emitting light at two test wavelengths of 1.142 $\mu\text{m}$  and 1.162 $\mu\text{m}$ . The result is shown in the left-hand side of Figure 15. The two in focus images are located in the center of the detector and appear as two small red dots, with a normalized intensity of 1. These two points of light are surrounded by an array of in focus ghost images, caused by stray light paths in the boundary area between lens 1 and lens 2, with intensity levels of up to 0.001. Fortunately we can easily block such stray light with the use of absorbing baffles around the lens 1 and lens 2 mounting interface.

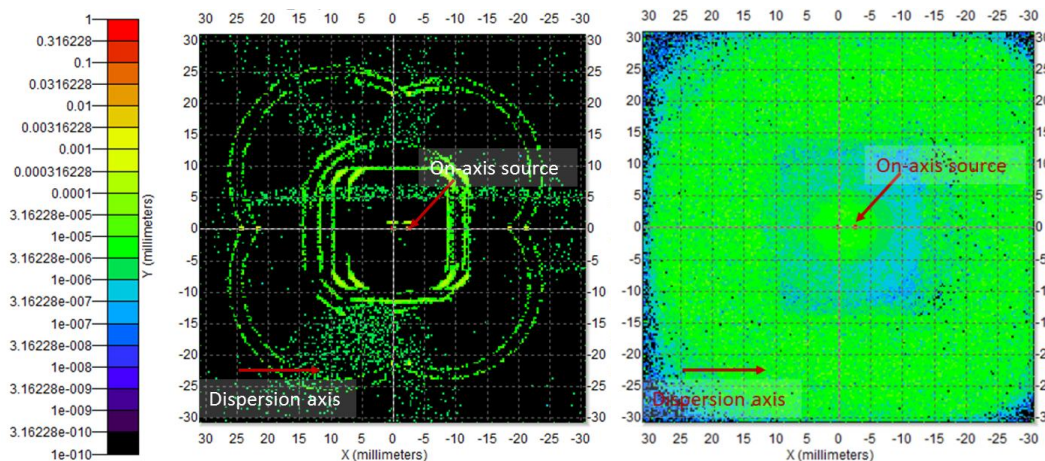


Figure 15 Irradiance plots at the MOONS detector for the YJ-band spectrograph, illuminated with an on-axis source at wavelength of 1.142  $\mu\text{m}$  and 1.162  $\mu\text{m}$ .

Following design of the baffle structures and inclusion into the TracePro model, we performed a further analysis to measure the background level of scattered light. The result is shown in the right-hand side of Figure 15. The two in focus images can still be seen at the center of the detector with a normalized intensity of 1, however now there is a background stray light level with a relative intensity of  $\sim 10^{-5}$ . A large fraction of this stray light is caused by the detector reflecting around 5% of the incident light back in to the spectrograph. This light then re-circulates with the spectrograph optical cavity and generates a diffuse background of scattered light filling the entire detector. Opto-mechanical design work is

currently under way to further improve the baffling within the MOONS spectrograph with the aim of reducing the scattered light level still further.

Ghost shapes and position also depends on fiber position and wavelength, so that we will finally compute a corresponding 4D ghost image cube to be interpolated for each spot position.

## 7. FINAL PSF MODEL

We finally merge all the described contribution into a comprehensive spot model for each grid location. This also considers the projected shapes of the fiber core, that we compute via IDL to ZEMAX interaction by displacing each field center to the x-y edge points of the 150 $\mu$ m core quadrants and computing the corresponding position of the chief ray on the focal plane. For simplicity, we assumed a projected elliptical shape parallel to x-y detector axes, which covers an area of about 3 $\times$ 3 pixels, and a flat-top profile for the illumination of the fiber output.

The final spot image  $S$ , for each field and wavelength position on the chosen grid, is thus the convolution of the diffraction-plus-aberration model  $A$ , described in Sec.4.2, with the fiber core projection  $F$ , in turn convolved with the ghost image  $G$  (Sec.6) and with the detector spread function  $D$  (Sec.5), and finally sampled by integration over the area of each pixel  $P_{xy}$ .

$$S_{xy} = \int_{P_{xy}} F \otimes A \otimes G \otimes D \quad (1)$$

In practice, though, we cannot do this computation as simply as written, because it would require a huge amount of memory and computation time, due to the micron-level resolution of the  $A$  model. We thus use an approximation, based on the fact that the different contributions to the PSF has different main spatial scales: the optical aberrations, the diffraction peak, and the base of the spikes have sharp features at micron scales, which needs sub-pixel sampling for the model  $A$ . The corresponding pixel sampling highly depends on where the PSF peak falls within the pixel area. On the contrary, the large-scale tails of the spikes, the wide diffraction halo, and the unfocused ghosts do not have sharp features at sub-pixel scale, so we can convolve them at the coarser pixels resolution without any significant loss of precision. Hence, we first compute the fine scale convolutions by displacing the spot center on a 5 $\times$ 5 grid of fractional pixel offsets, thus building a 6D image cube, i.e. a pixel sampled PSF image for each field, wavelength, and fractional x and y offsets. Then, when building the final spectral image, we linearly interpolate this 6D cube and convolve the result with the interpolated coarse scale components, i.e. the ghosts and the halo. This task, repeated for each wavelength and fiber, finally produces the photon image at the focal plane, to which the detector readout is finally applied, giving the raw image in Figure 2.

## ACKNOWLEDGEMENTS

We thanks Dr. Lorenzo Busoni (INAF) for having kindly provided us with its zmxIDL code<sup>[4]</sup>, which allows ZEMAX commanding from IDL. We also acknowledge the financial support from the “TECNO INAF 2014”<sup>[17]</sup> italian funds (P.I. Andrea Bianco).

## REFERENCES

- [1] Li Causi, G., Cabral, A., Ferruzzi, D., Finger, G., Giacalone, G., Guinouard, I., Lorenzetti, D., Oliva, E., Pedichini, F., Royer, F, Todd, S., Vitali, F., "Virtual MOONS: a focal plane simulator for the MOONS thousand-fiber NIR spectrograph." Proc. SPIE. 9147, Ground-based and Airborne Instrumentation for Astronomy V, 914764 (2014)

- [2] Taylor, W. D., Cirusuolo, M., Afonso, J., et al., "Virtual MOONS: a focal plane simulator for the MOONS thousand-fiber NIR spectrograph." Proc. SPIE. 9908, Ground-based and Airborne Instrumentation for Astronomy VI, 990860 (2016)
- [3] Oliva, E., Delabre, B. A., Tozzi, A., Ferruzzi, D., Lee, D., Parry, I. R., Rees, P., " The MOONS-VLT Spectrometer: toward the final design." Proc. SPIE. 9908, Ground-based and Airborne Instrumentation for Astronomy VI, 9908290 (2016)
- [4] Busoni L., "zmxIDL, an IDL toolbox to communicate with ZEMAX", <https://github.com/lbusoni/zmxIDL>
- [5] Exelis Visual Information Solutions, Inc., "IDL, Interactive Data Language", <http://www.harrisgeospatial.com/ProductsandSolutions/GeospatialProducts/IDL/Language.aspx>
- [6] Zemax, LLC., <http://www.zemax.com/>
- [7] Holland, S., "Fully depleted, back-illuminated CCDs for astronomy and astrophysics", 2012, [http://microlab.berkeley.edu/text/seminars/slides/holland\\_sep2012.pdf](http://microlab.berkeley.edu/text/seminars/slides/holland_sep2012.pdf)
- [8] HAWAII 4RG™, IR and Visible FPA, <http://www.teledyne-si.com/ps-h4rg.html>
- [9] Oliva E., et al., "Updated optical design of the MOONS-VLT spectrometer" Proc. SPIE 9147-84, Ground-based and Airborne Instrumentation for Astronomy, (June 23, 2014)
- [10] Sullivan P.W. and Simcoe R.A., "A Calibrated Measurement of the Near-IR Continuum Sky Brightness Using Magellan/FIRE" PASP, Vol. 124, No. 922 (December 2012), pp. 1336-1346
- [11] Wilson J.C., et al., "Performance of the Apache Point Observatory Galactic Evolution Experiment (APOGEE) high-resolution near-infrared multi-object fiber spectrograph" Proc. of SPIE Vol. 8446
- [12] Li Causi, G., Giacalone, G., "Diffraction profiles from a grating with circular aperture", [https://livelink.roe.ac.uk/Livelink/livelink.exe?func=ll&objId=9311603&objAction=Open&nexturl=%2FLivelink%2Flivelink%2Eexe%3Ffunc%3D%26objAction%3DBrowse%26objType%3D900%26id%3D8819463%26nextUrl%3D%26f\\_8977629%3D144](https://livelink.roe.ac.uk/Livelink/livelink.exe?func=ll&objId=9311603&objAction=Open&nexturl=%2FLivelink%2Flivelink%2Eexe%3Ffunc%3D%26objAction%3DBrowse%26objType%3D900%26id%3D8819463%26nextUrl%3D%26f_8977629%3D144) (restricted access).
- [13] ALTA U9000 CCD, <http://www.narit.or.th/files/U9000.pdf>
- [14] Zanutta, A., Bianco, A., Insausti, M., Garzón, F., "Volume phase holographic gratings for astronomy based on solid photopolymers" Proc. SPIE. 9151, Advances in Optical and Mechanical Technologies for Telescopes and Instrumentation, 91515 (2014)
- [15] O'Connor, P., Radeka, V.; Figer, D.; Geary, J. G.; Gilmore, D. K.; Oliver, J.; Stubbs, C. W.; Takacs, P. Z., and Tyson, J. A., "Study of silicon thickness optimization for LSST" Proc. SPIE 6276, High Energy, Optical, and Infrared Detectors for Astronomy II, 62761W (2006)
- [16] TracePro, <http://www.lambdare.com/tracepro>
- [17] Bianco, A., et al., "Innovative tools for high resolution and infrared spectroscopy based on non-standard volume phase holographic gratings" BANDO\_TECNO-INAF 2014, (2014)